Incorporation of Boron in Mesoporous Bioactive Glass Nanoparticles Reduces Inflammatory Response and Delays Osteogenic Differentiation

Kai Zheng,* Yuqian Fan, Elisa Torre, Preethi Balasubramanian, Nicola Taccardi, Clara Cassinelli, Marco Morra, Giorgio Iviglia, and Aldo R. Boccaccini*

Mesoporous bioactive glass nanoparticles (MBG) are multifunctional building blocks for tissue regeneration and nanomedicine applications. Incorporation of biologically active ions can endow MBG with additional functionalities toward promoted therapeutic effects. Here, boron is incorporated into MBG by using a sol–gel approach. The concentration of boron incorporated is controllable by tuning the amount of boron precursor. Two types of boron-doped MBG, namely 10B- and 15B-MBG (5.8 and 6.5 mol% of B_2O_3, respectively) are synthesized. Boron incorporation does not significantly influence the particle morphology. All synthesized particles exhibit a sphere-like shape with a size ranging from 100 to 300 nm. 10B- and 15B-MBG show large specific surface area (346 and 320 m^2 g^{-1}, respectively) and pore volume. Both boron-doped MBG exhibit remarkable in vitro bioactivity and noncytotoxicity. Boron incorporation is shown to reduce the inflammatory response linked to macrophages as indicated by downregulated expression of pro-inflammatory genes. However, boron incorporation delays the osteogenic differentiation in osteoblasts as indicated by the downregulated expression of pro-osteogenic genes. The results demonstrate the promising potential of using boron-doped MBG to modulate inflammatory response for bone regeneration under inflammatory conditions, as shown in this study for the first time.

1. Introduction

With the development of modern medical treatments, the healing of bone defects has been tremendously improved. However, some clinical problems, such as lack of vascularization, infection and unregulated inflammatory reaction, are still challenges for achieving successful bone defect healing.[1] Biomaterials capable of providing osteogenic and angiogenic conditions as well as showing antimicrobial activity are expected to greatly promote the healing of bone defects that suffer from the aforementioned conditions.[1,2] Among various promising inorganic biomaterials being used for bone healing applications, bioactive glasses (BG) are attracting increasing attention for healing large or infected bone defects, considering their capability to induce osteogenic and angiogenic activities.[3] Since the discovery of the first BG, 45S5 Bioglass,[4] numerous BG of novel chemical composition and morphology have been developed for promoting bone regeneration.[5] Advances of sol–gel chemistry enable the control of BG morphology on the nanoscale,[6] leading to the development of BG based thin coatings,[7] nanoparticles[8] and nanoscale fibers,[9] which make the applications of nanoscale BG in bone repair, wound healing, and nanomedicine possible.[5,10] Particularly, mesoporous bioactive glass nanoparticles (MBG) emerge as promising bioactive fillers and drug delivery platforms for these applications, due to their tunable small particle size and porosity as well as large specific surface area and pore volume.[6,11] MBG can also induce synergistic effects of biologically active ions and loaded biomolecules (e.g., antibiotics, growth factors) toward promoted therapeutic action by locally releasing them in a controlled manner.[12]

Dissolution products of BG are key to induce specific therapeutic action, as the released ions can interact with

Dr. K. Zheng, Y. Fan, Dr. P. Balasubramanian, Prof. A. R. Boccaccini
Institute of Biomaterials
University of Erlangen-Nuremberg
Cauerstrasse 6, Erlangen 91058, Germany
E-mail: kai.zheng@fau.de; aldo.boccaccini@fau.de

Dr. E. Torre, Dr. C. Cassinelli, Dr. M. Morra, Dr. G. Iviglia
Nobil Bio Ricerche Srl
Via Valcastellana 26, Portacomaro AT 14037, Italy

Dr. N. Taccardi
Institute of Chemical Reaction Engineering
University of Erlangen-Nuremberg
Egerlandstraße 3, Erlangen 91058, Germany

**ADVANCED
SCIENCE NEWS**

www.advancedsciencenews.com

Particle
& Particle Systems Characterization

www.particle-journal.com

genes, proteins, and cells to induce positively biological functionalities.[13] Boron plays an important role in many biological processes in the human body, such as embryogenesis, bone growth, and maintenance.[14] Recently, the study of the effects of boron on stimulating bone regeneration and wound healing has started to attract increasing attention.[13–15] For example, borate BG have shown their capability to accelerate the healing of chronic wounds, mainly due to their great surface reactivity and released boron ions.[16,17] As a potent regulator of osteogenesis and angiogenesis, boron incorporated in BG can also promote biological performances toward enhanced bone tissue regeneration.[15] Boron doped nonporous BG nanoparticles have been produced using sol–gel based methods for bone repair or dental applications.[18,19] However, the synthesis of pure borate BG nanoparticles is still challenging due to the low chemical durability of such particles.[20] To the best of the authors' knowledge, the development of boron-doped MBG for biomedical applications has not been reported, even though this type of nanoparticles has great advantages as bioactive fillers or building blocks for medical devices being able to simultaneously deliver boron ions and biomolecules. Development of boron-containing MBG is thus of great interest for fabricating BG based medical devices in various biomedical applications.

The biological effects of BG nanoparticles, for example osteogenesis and angiogenesis in the context of tissue engineering, have been extensively investigated.[21,22] However, the influence of BG nanoparticles on inflammatory response has been rarely reported.[23–25] Many efforts have been dedicated to reducing the inflammatory response induced by BG. For example, surface functionalization with biomolecules has been used to reduce inflammatory response.[24] Alternatively, doping of specific ions (e.g., Ce) into BG can also reduce inflammatory response, mainly due to the antioxidant activity of the ions.[25] Importantly, osteogenesis and angiogenesis effects induced by BG can also be promoted by modulating inflammatory response.[23,24] Dietary boron has been reported to be able to suppress inflammatory response.[26] For example, it has been reported that incorporation of boron into calcium silicate coatings induced a significantly reduced expression of pro-inflammatory cytokines and an increased expression of anti-inflammatory cytokines.[27] However, the influence of boron incorporation in MBG on inflammatory response has not been investigated even though the therapeutic effect of boron has been considered for tissue regeneration applications, as mentioned above.

In this work, boron-containing silicate MBG were successfully synthesized by using a microemulsion assisted sol–gel approach. The influence of boron incorporation on particle morphology, pore structure, chemical structure, and bioactivity was investigated. Cellular responses induced by boron-doped MBG, in terms of cytotoxicity, inflammatory response, and pro-osteogenic activities, were evaluated. The results reveal that boron incorporation in the investigated concentrations can reduce the inflammatory response induced by MBG but it delays osteogenic differentiation.

2. Results and Discussion

In this study boron-free and boron-containing MBG were produced by using a microemulsion assisted sol–gel approach that

has shown the capability to synthesize mesoporous nanoparticles of different morphologies and chemical compositions.[28–31] As shown in the schematic diagram of the MBG synthesis (**Figure 1**a), ethyl acetate was used to form oil-in-water microemulsion droplets as the templates of nanoparticles while CTAB acted as the template guiding the formation of mesopores. Figure 1b shows the size distribution of the particles measured by the dynamic light scattering (DLS) technique. All particles exhibited relatively narrow size distributions. The average sizes of MBG, 10B-, and 15B-MBG were 250, 194, and 211 nm, respectively. The addition of boron seemed to slightly reduce the average size of the nanoparticles. The zeta potential values were measured to be −24, −27, and −31 mV for MBG, 10B-, and 15B-MBG, respectively. The negative surface charge of these nanoparticles, evidenced by the zeta potential values, was attributed to the silanol groups on the particle surfaces being deprotonated.[32] Figure 1c shows SEM images of MBG, 10B-, and 15B-MBG, where all particles exhibit a sphere-like shape. Moreover, no obvious aggregated nanoparticles are observed in these SEM images. TEM images (Figure 1d) showed the presence of mesopores in these particles, which was induced by the removal of CTAB templates during calcination. The sizes of all particles are observed to be in the range of 100–300 nm. In addition, the shape of the particles does not look completely spherical. Ellipsoidal particles can also be observed, which can explain the relatively wide size distribution results obtained by DLS measurement. The particle sizes of 10B- and 15B-MBG were slightly smaller than that of MBG, in agreement with the DLS results, confirming that incorporation of boron slightly influenced the particle size. On the other hand, the shape of the particles and formation of mesopores were not significantly affected, which is consistent with previous results reporting that the addition of appropriate precursors during the microemulsion assisted sol–gel process does not interfere with the formation of morphologically homogeneous particles.[29,30]

Figure 2 shows the results of nitrogen sorption isotherms and pore size distribution. All the particles exhibited a type IV nitrogen isotherm with an H3 hysteresis loop (Figure 2a) as defined by IUPAC, indicating the presence of mesopores with slit-shaped pores, which is consistent with TEM observation (Figure 1d). Boron-free MBG displayed a relatively narrow pore size distribution centered at 2.9 nm (Figure 2b). However, boron incorporation seemed to enlarge the pore size of the particles, as both 10B- and 15B-MBG displayed wider pore size distribution centering at 5.6 and 7.7 nm, respectively. The enlarged pore size in boron-containing MBG could also be observed in TEM images (Figure 1d). Particularly, larger and irregular pores could be observed in the TEM image of 15B-MBG. The specific surface area of MBG, 10B-, and 15-MBG was 424, 346, and 320 m² g⁻¹, respectively. It seems that boron incorporation reduced the specific surface area of the particles, but enhanced the pore volume as evidenced by the increased pore volume from 0.36 (MBG) to 0.38 (10B-MBG) and 0.42 cm³ g⁻¹ (15B-MBG). The change in pore morphology after boron incorporation can be attributed to the interaction between boric acid and CTAB/TEOS. Boric acid could react with water molecules to form $B(OH)_4^-$ anion and H_3O^+ cation, which is expected to further affect the self-assembly of cationic CTAB molecules.

**ADVANCED
SCIENCE NEWS**

www.advancedsciencenews.com

Particle
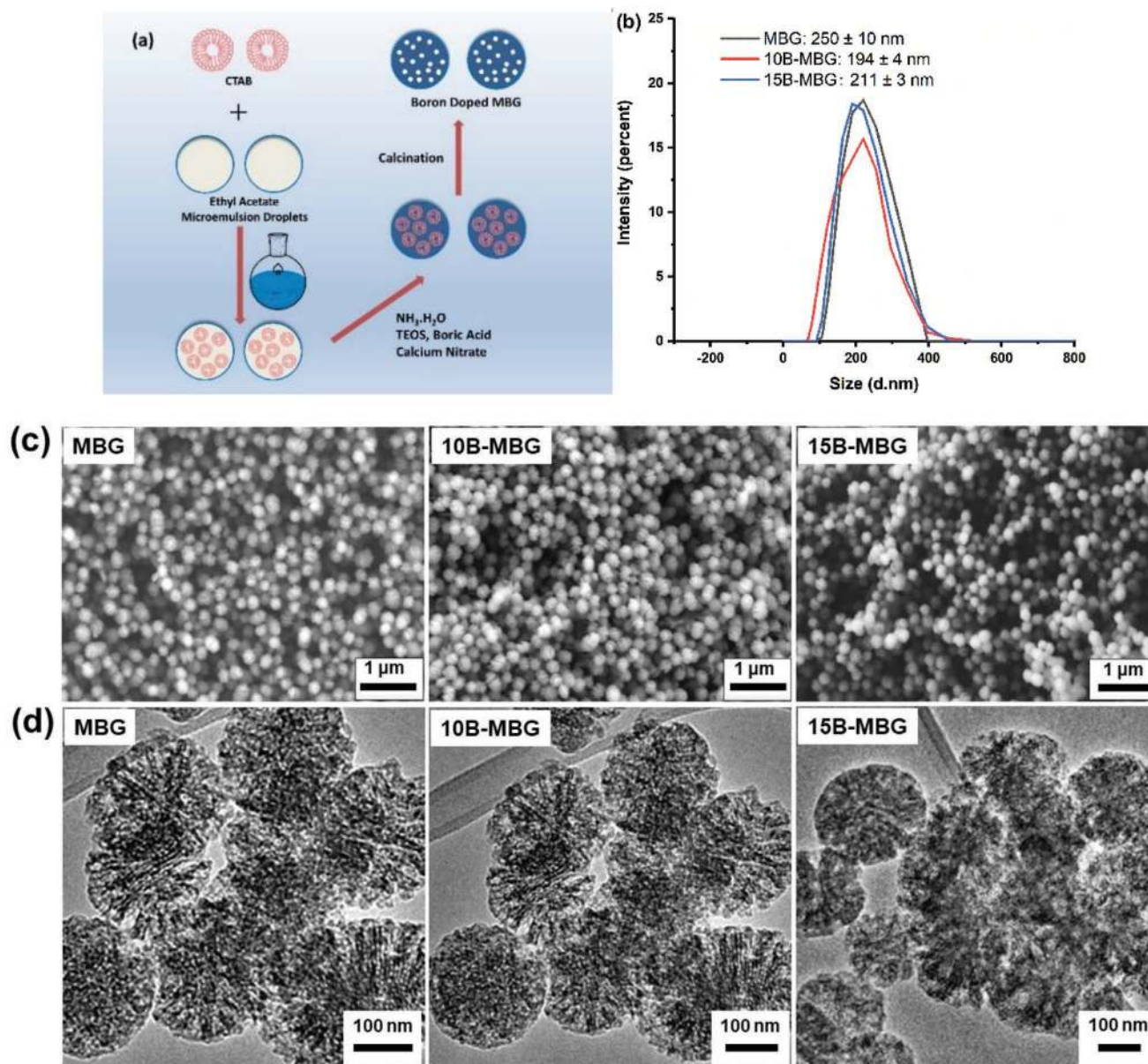& Particle Systems Characterization

www.particle-journal.com

Figure 1. a) Schematic illustration of the sol–gel synthesis process; b) particle size distribution obtained by DLS measurements, c) SEM images and d) TEM images of MBG, 10B-MBG, and 15B-MBG.

Also, the presence of boric acid could affect the solution pH, which could affect the formation of mesophases.[33,34] Therefore, both the pore structure and particle morphology of MBG changed after the addition of boric acid. It has been known that particle size, particle shape, and pore structure of nanoparticles could be controlled by adjusting the concentration of catalysts, TEOS and ethyl acetate in the microemulsion assisted sol–gel process.[28,35] The results showed here indicate that the control of boric acid addition could also tune the morphology of the resulting nanoparticles. For example, by carefully controlling this interaction, Yang et al.[33] have prepared mesostructured silica with tailorable particle morphology from hollow spheres to hierarchical assembly and mesoporous structures. Nevertheless, the incorporation of boron maintained the nanoscale

particle size, high specific surface area, and large pore volume of MBG, which are expected to facilitate the potential biomedical applications of boron-containing MBG in drug delivery and bone regeneration.[12]

Table 1 displays the nominal and actual (in bracket) chemical compositions of MBG and boron-containing MBG. The results confirmed the successful incorporation of boron into 10B- and 15-MBG that contained approximately 5.8 and 6.5 mol% of B_2O_3, respectively. For sol–gel derived BG nanoparticles, a gap between the nominal and actual chemical compositions is usually present. The concentration of target ions (e.g., Ca, Cu) incorporated in BG nanoparticles is usually lower than the designed or nominal concentration.[6,30,36] It is challenging to predict the actual concentration of target ions incorporated in
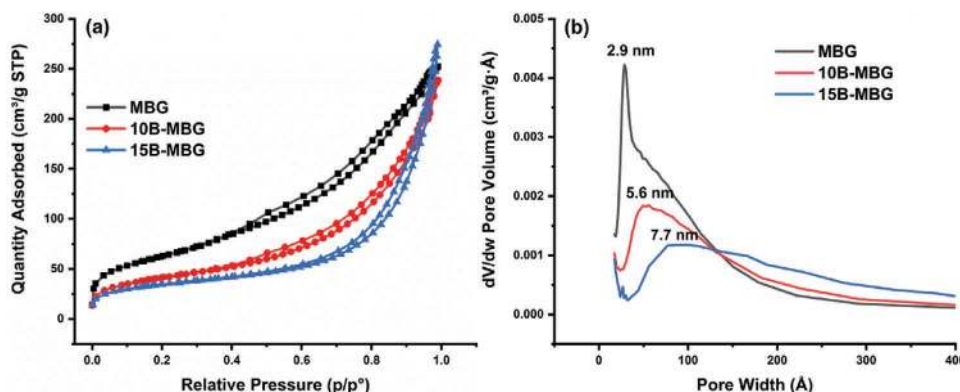
**ADVANCED
SCIENCE NEWS**
www.advancedsciencenews.com

Particle
& Particle Systems Characterization
www.particle-journal.com

Figure 2. a) Nitrogen sorption isotherms and b) the pore size distribution of MBG, 10B-MBG, and 15B-MBG.

BG nanoparticles from the nominal composition. In the present study, relatively high concentrations of B_2O_3 (10 and 15 mol%) were selected for synthesizing boron-containing MBG to avoid too low concentrations of B_2O_3 incorporated in the resulting particles. Although the actual concentrations of B_2O_3 were lower than the nominal ones, relatively high concentrations of incorporated B_2O_3 were achieved. The gap between the nominal and actual compositions was also observed in boron-free MBG. Approximately 11 mol% of Ca was incorporated into MBG, far lower than the designed 40 mol%. Such a chemical composition gap could be explained by the formation mechanism of nanoscale BG in the sol–gel process.[8,32,37] During the formation of nanoparticles, those ions (e.g., Ca^{2+}) that do not contribute to the silicate network are adsorbed on the surface of colloidal silica nanoparticles first and then enter the silicate network by diffusion during heating treatments.[8,32,38] Thus, the amount of incorporated ions depends on the adsorption capacity of silica nanoparticles, which can be influenced by the specific surface area of nanoparticles, pH, and temperature.[32] Boric acid could directly interact with Si-OH to form the Si—O—B bond but this bonding could be easily hydrolyzed.[33] The unstable Si—O—B bond results in the easy removal of boron during the post-treatment process (e.g., washing) and calcination, which also contributes to the lower concentration of boron in MBG. It is thus difficult to incorporate high amounts of ions into the nanoparticles because such high concentrations could exceed the ion adsorbing capacity of silica nanoparticles.[32] Although precise control of the concentration of doped boron is challenging, the present results showed that the concentration of boron in MBG could be tailored by controlling the amount of boron precursor (in this case boric acid).

Figure 3a shows FTIR spectra of MBG, 10B-, and 15B-MBG. All the particles exhibited characteristic bands of silicate

glasses. Two bands located at 438 and 804 cm^{-1} could be assigned to Si—O—Si bending and symmetric stretching vibrations, respectively, while the band located at 1021 cm^{-1} and a shoulder at 1232 cm^{-1} could be assigned to Si–O–Si asymmetric stretching mode and $[SiO_4]$ tetrahedral, respectively.[39] The band at 1647 cm^{-1} was induced by molecular water.[40] Observation of these bands indicates the silicate network of the particles.[39] Compared to boron-free MBG, 10B-, and 15B-MBG showed a shoulder located at 936 cm^{-1} that could be assigned to the stretching vibration of B–O from BO_4 units.[18,40] Also, two new bands located at 1386 and 678 cm^{-1} were observed in the spectra of 10B- and 15B-MBG, which could be ascribed to the B–O–B stretching vibrations of $[BO_3]$ units and B—O—Si bond, respectively.[18,20,34] FTIR results verified the existence of boron and the formation of B—O—Si bonding in 10B- and 15B-MBG. It is known that the addition of B_2O_3 to silicate glasses can lead to the breakup of the 3D Si–O–Si network resulting in the formation of $[BO_3]$ trihedral or chains of $[BO_3]$ triangles.[41] However, it seems that boron in 10B- and 15B-MBG mainly existed in the form of B–O–B rather than B–O–Si linkages, as indicated by the weak FTIR bands related to B–O–Si linkages, which could be due to the unstable nature of the Si—O—B bond.[20,33] XRD results (Figure 3b) confirmed the amorphous nature of all nanoparticles as only characteristic broad bands of amorphous silicate materials could be observed. Also, no diffraction peaks related to boric acid crystals could be observed, which suggests the incorporation of boron into MBG as well as the chemical homogeneity of boron-containing MBG. It can thus be concluded that boron-containing MBG can be successfully synthesized using the microemulsion assisted sol–gel approach presented here with boric acid being an effective precursor for incorporating boron into silicate BG.

Figure 3c,d shows ion release profiles of MBG, 10B-, and 15B-MBG in Tris-HCl buffer solution. All nanoparticles showed a burst release of Ca ions within 24 h (Figure 3a), while the concentrations of released Ca ions of all nanoparticles appeared to be stable after 48 h in Tris-HCl. 15B-MBG seemed to release a higher concentration of Ca ions in comparison to MBG and 10B-MBG, both of which showed a similar release profile. Moreover, both 10B- and 15B-MBG exhibited similar B ion release profiles. Similarly, 15B-MBG could release a higher concentration of B ions than 10B-MBG. It has been reported that mesoporous BG nanoparticles could degrade in physiological fluids over

Table 1. Nominal and actual compositions (mol%) of MBG, 10B-, and 15B-MBG. The actual compositions of the particles were determined by ICP-AES.

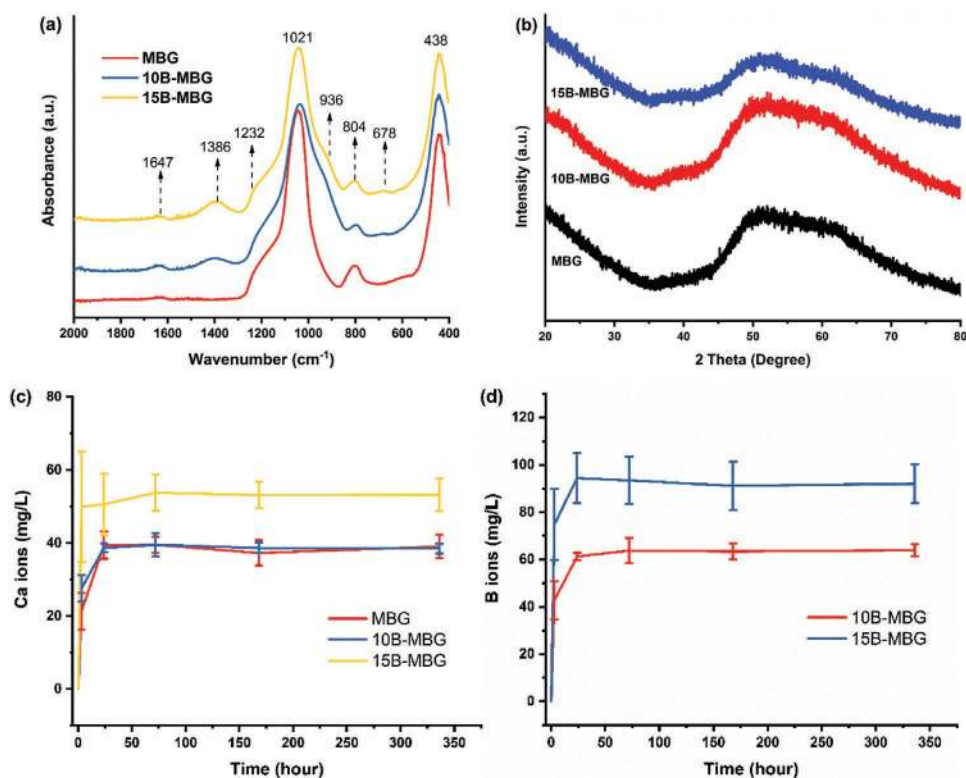| Designation	SiO_2	CaO	B_2O_3
MBG	60 (88.9 ± 3.3)	40 (11.1 ± 0.4)	0
10B-MBG	50 (82.9 ± 1.8)	40 (11.3 ± 0.8)	10 (5.8 ± 0.3)
15B-MBG	50 (83.9 ± 3.2)	35 (9.6 ± 0.2)	15 (6.5 ± 0.3)

2000054 (4 of 12)

Figure 3. a) FTIR spectra and b) XRD patterns of MBG, 10B-, and 15B-MBG. c,d) Ion release profiles of the nanoparticles in Tris-HCl (pH 7.4) at 37 °C.

time.[25,30] During degradation, these nanoparticles release ions that can induce specific cellular activities depending on the type and concentrations of the ions.[13] Understandably, 15B-MBG could release a larger amount of B ions than 10B-MBG, given the higher concentrations of B_2O_3 in the chemical composition (Table 1). Moreover, because of the higher concentration of B_2O_3 in 15B-MBG, these nanoparticles have more Si—O—B bands in their silicate structure. However, this bonding can be easily hydrolyzed, which facilitates the leaching of boron ions and the degradation of nanoparticles in aqueous solutions.[33] This mechanism can also explain the slightly larger amount of Ca ions released from 15B-MBG in comparison to MBG and 10B-MBG.

The influence of boron on the in vitro hydroxyapatite (HA) forming ability of MBG, an important characteristic that indicates the bone-bonding capability of bioactive materials,[42] was investigated. **Figure 4**a shows FTIR spectra of MBG, 10B-, and 15B-MBG after soaking in SBF for up to 14 days. Characteristic bands related to silicate groups located at 1232, 1021, 804, and 438 cm^{-1} were still present after soaking in SBF, indicating that the particles were not fully dissolved after 14 days. For boron-containing MBG, the bands related to borate groups located at 678 and 1386 cm^{-1} disappeared while the band at 936 cm^{-1} ascribed to B–O stretching vibration could still be observed after soaking in SBF for 1 day. However, this band also disappeared after 3 days in SBF. This phenomenon suggested the release of BO_3^{3-} from boron-containing MBG and the collapse of the borate structure in these particles. A new peak located at 560 cm^{-1}, representative of P–O bending vibration in tetrahedral [PO_4], appeared in the FTIR spectra of 10B- and 15B-MBG after soaking in SBF for 1 day, but this peak was not observed in the

FTIR spectrum of MBG. After 3 days of soaking in SBF, another peak located at 604 cm^{-1}, also ascribed to P–O bending vibration in tetrahedral [PO_4], appeared in the FTIR spectra of MBG and 10B-MBG to form double peaks. However, the formation of the double peaks was only observed in the FTIR spectrum of 15B-MBG after 7 days in SBF. Although the presence of these two peaks did not confirm HA formation, they could indicate the presence of orthophosphate lattices that are well recognized as an indicator of HA.[43] Another new peak located at 960 cm^{-1} related to symmetric stretching of orthophosphate PO_4^{3-} group[39] could be observed in the FTIR spectra of all particles after 3 days of soaking in SBF. Also, a peak at 876 cm^{-1} assigned to carbonate group CO_3^{2-} could be observed in the spectra of all particles after soaking in SBF for 14 days, suggesting that the formed HA could be converted to carbonated HA (bone-like HA) during the soaking in SBF.[43] Moreover, the intensity of these phosphate-related peaks became greater with increasing soaking time, suggesting the increased amount and crystallinity of the formed HA. SEM images (Figure 4b) of these particles after soaking in SBF for 14 days showed the characteristic needle-like morphology of HA crystals,[30] providing visual evidence of the HA forming ability of the particles. Figure 4c shows XRD patterns of these particles after soaking in SBF. After 3 days in SBF, no diffraction peaks could be detected probably due to a small amount of formed HA crystals. After 7 days of soaking, diffraction peaks ascribed to HA crystals could be observed in XRD patterns of all particles, but the detected peaks were different in these particles. After 14 days of soaking, the peaks assigned to (002) and (211) crystallographic planes of HA (ICDD PDF 2 01-089-4405) could be seen in XRD patterns of 10B- and 15B-MBG, while
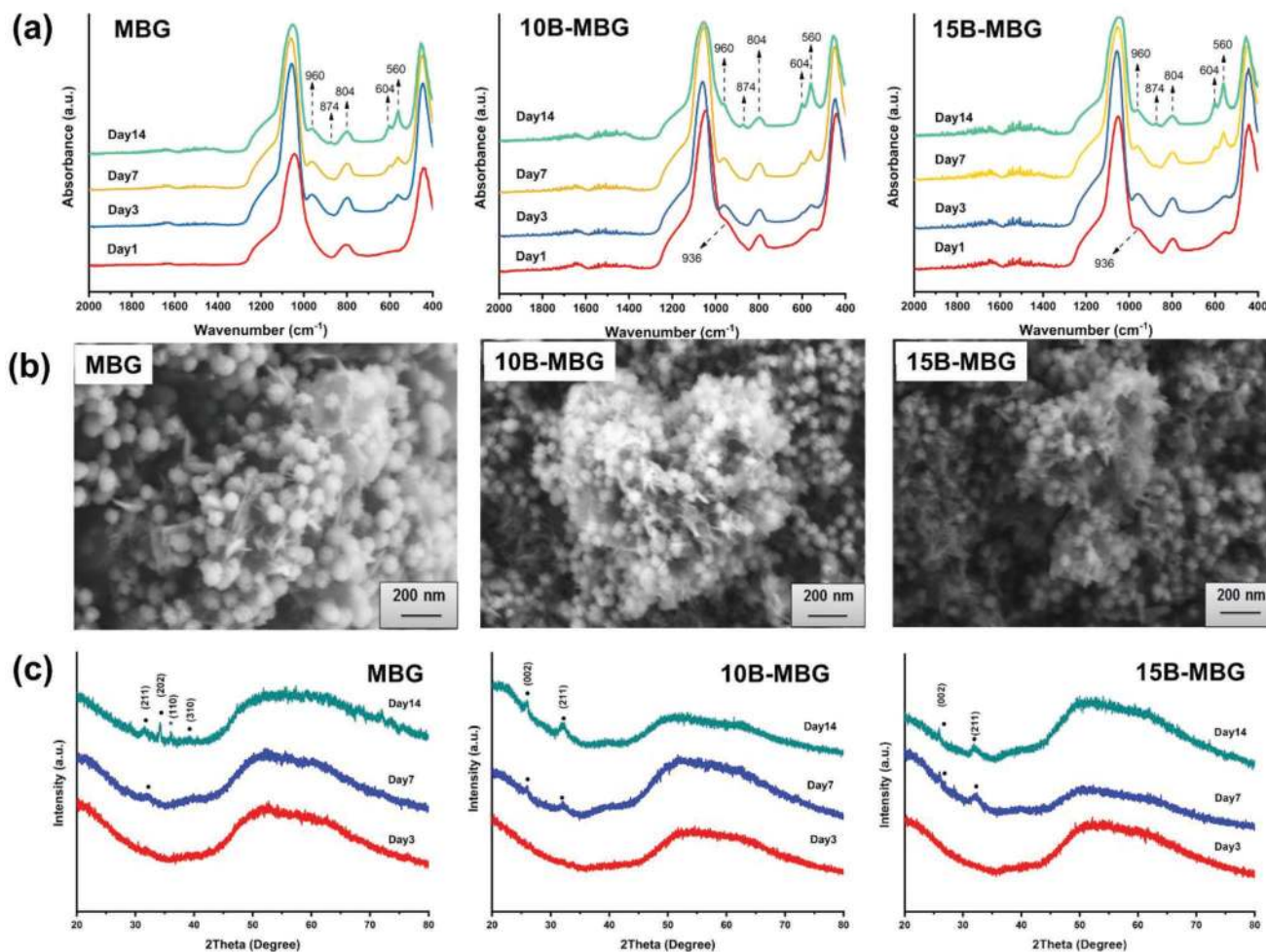
**ADVANCED
SCIENCE NEWS**
www.advancedsciencenews.com

Particle
& Particle Systems Characterization
www.particle-journal.com

Figure 4. Evaluation of in vitro HA formation ability of MBG, 10B-, and 15B-MBG. a) FTIR spectra of particles after soaking in SBF for up to 14 days; b) SEM images of particles after soaking in SBF for 14 days; c) XRD patterns of particles after soaking in SBF for up to 14 days (● indicates HA and * indicates calcite).

those assigned to (211), (202), and (310) crystallographic planes could be observed in MBG.[44] Also, the peak related to (110) crystallographic plane of calcite could be found in the XRD pattern of MBG. It has been reported that calcite could be formed on nanoscale BG after soaking in SBF likely due to an excessive amount of Ca ions released in SBF resulting in a higher Ca/P ratio and a pH shift.[45] The effects of boron incorporation on the bioactivity of BG have been extensively investigated as reviewed in the literature.[15] Generally, the addition of boron in silicate glass compositions can enhance the dissolution of glasses and therefore promotes bioactivity.[15] In our study, the FTIR results indicated that the incorporation of boron seemed to facilitate the initial formation of HA at the early stage of soaking in SBF, probably due to the faster dissolution of boron-containing MBG.[41] However, no significant influence of boron on further formation and growth of HA was observed. Nevertheless, all particles (MBG, 10B- and 15B-MBG) exhibited rapid HA forming ability that is favorable for applications related to bone repair/regeneration (e.g., bone scaffolds, orthopedic coatings).

Figure 5a shows the relative viability of ST2 cells cultured with the particles. At the concentration of 10 mg mL^{-1}, all the particles reduced the relative cell viability in comparison to the control. Particularly, 10B- and 15B-MBG exhibited viability lower than 70% indicating their cytotoxicity at this concentration according to the international standard ISO 10993-5: 2009-Biological. At diluted concentrations (1 and 0.1 mg mL^{-1}), all particles showed no reduced cell viability in comparison to the control. Notably, at the concentration of 1 mg mL^{-1}, the 10B-MBG group exhibited significantly higher cell viability than that of the control and boron-free MBG groups. No significant difference in cell viability between MBG and boron-containing MBG groups could be observed at the concentration of 0.1 mg mL^{-1}. It has been reported that relatively higher concentrations of Ca^{2+} and $(BO_3)^{3-}$ could induce cytotoxicity,[30,46] which could explain the reduced cell viability at the concentration of 10 mg mL^{-1}. At the diluted concentrations, boron-containing MBG did not reduce the cell viability in comparison to the control, while 10B-MBG could even increase the cell viability at the concentration of 1 mg mL^{-1}. Figure 5b shows light microscopy images of H&E-stained ST2 cells cultured with the nanoparticles at different concentrations. At the concentration of 10 mg mL^{-1}, the cell density was significantly reduced in all nanoparticle groups
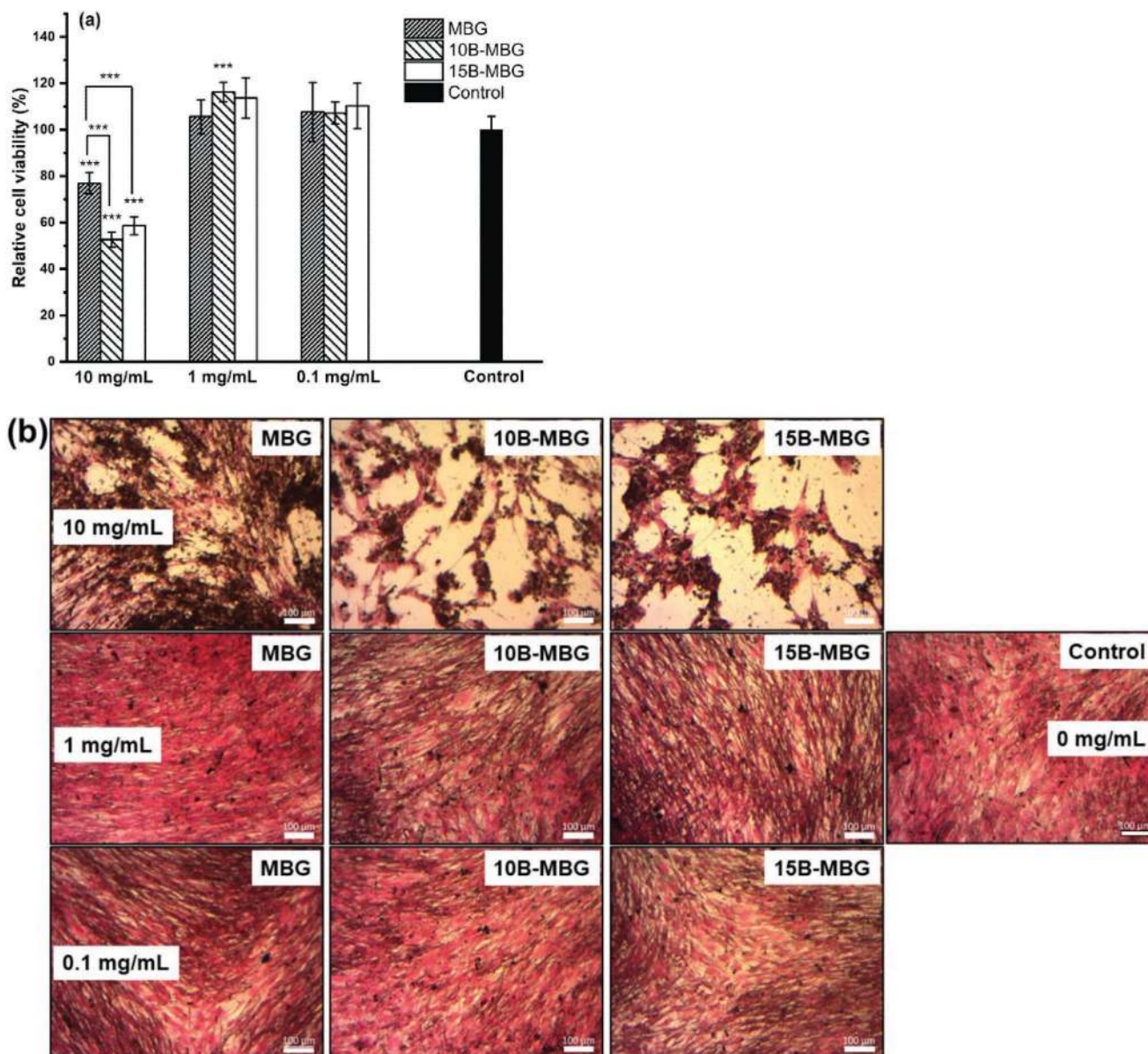
**ADVANCED
SCIENCE NEWS**

www.advancedsciencenews.com

Particle
& Particle Systems Characterization

www.particle-journal.com

Figure 5. a) Relative viability of ST2 cells cultured with MBG, 10B-, and 15B-MBG at concentrations of 10, 1, and 0.1 mg mL^{-1}. b) Light microscopy images of H&E-stained ST2 cells cultured with the particles at different concentrations.

as compared to the control group, which indicated cytotoxicity induced by the nanoparticles at this concentration. In addition, the remaining particles could be observed around the cells as indicated by black dots in the images. At the diluted concentrations of 1 and 0.1 mg mL^{-1}, no significant difference in cell density could be observed between the nanoparticle groups and the control, indicating noncytotoxicity of nanoparticles at these concentrations, which is consistent with the result of cell viability tests (Figure 5a). Taken together, the cell viability results and H&E staining images indicated no cytotoxicity of MBG, 10B-, and 15B-MBG at the concentrations of 1 and 0.1 mg mL^{-1}. Therefore, the concentration of 1 mg mL^{-1} was chosen for further cell biology studies to understand interactions between the nanoparticles and specific cells.

Figure 6a shows the results from RTqPCR analysis performed on macrophages incubated with the particles for 4 h at the concentration of 1 mg mL^{-1}. An overall significantly upregulated expression of pro-inflammatory genes mouse interleukin-1β (IL-1β), interleukin-6 (IL-6), tumor necrosis factor-alpha (TNFα) was observed, as compared to the control. However, the presence of boron induced a decrease in the extent of IL-1β and IL-6 expression, statistically significant for IL-6, as compared to MBG. The viability of ST2 cells was not affected by the particles at the concentration of 1 mg mL^{-1}, but MBG and boron-containing MBG were shown to induce inflammatory response in macrophages as compared to the control. It has been reported that silica-based nanoparticles could induce pro-inflammatory response by generating reactive oxygen species (ROS),[47] which
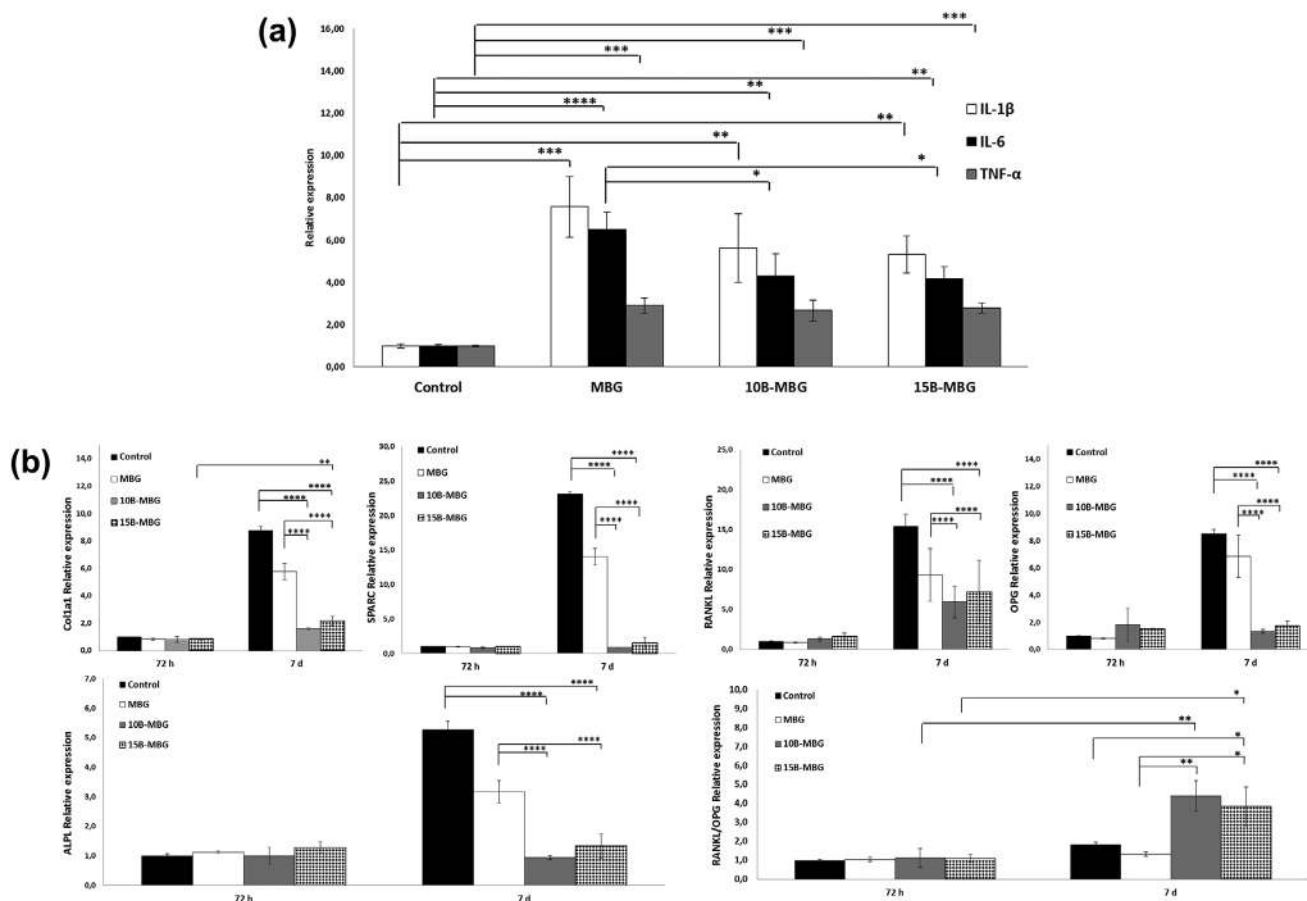
Figure 6. a) RTqPCR analysis of pro-inflammatory genes IL-1β, IL-6, and TNFα in macrophages incubated with MBG and boron-containing MBG for 4 h at the concentration of 1 mg mL^{-1}. The results obtained in the control group were treated as the relative group to obtain the relative expression results. b) RTqPCR analysis of pro-osteogenic genes COL1A1, ALPL, SPARC, RANKL, OPG, and RANKL/OPG in osteoblast-like SaOS2 cells incubated with MBG and boron-containing MBG at the concentration of 1 mg mL^{-1} for 72 h and 7 days. The relative group for osteogenic gene expression was the result of the control group obtained at 72 h. Data are expressed as mean ± SD. P values ≤0.05 were considered to be statistically significant (*p ≤ 0.05; **p ≤ 0.01; ***p ≤ 0.001; ****p ≤ 0.0001).

could explain the upregulated expression of pro-inflammatory genes by MBG, 10B-, and 15B-MBG in comparison to the control. Boron has been shown to inhibit oxidative stress and therefore reduce inflammatory responses,[48] which could explain the downregulated expression of IL-1β and IL-6 when boron was incorporated into MBG. Previous studies covering boron-containing BG mainly focused on overall osteogenic response underlined by osteoblast proliferation, expression of osteoblast specific markers and angiogenic mediators.[15] However, the influence of boron on inflammatory responses of cells has not gained adequate attention. Our results suggest that the incorporation of boron in BG could be a feasible strategy to modulate the inflammatory response that plays an important role in the healing of bone defects. Boron containing MBG represent promising bioactive materials for applications related to bone repair/regeneration under inflammatory conditions.

Figure 6b shows the expression of pro-osteogenic genes collagen 1A1 (COL1A1), receptor activator of nuclear factor kappa-B ligand (RANKL), secreted protein acidic and cysteine rich (SPARC), osteoprotegerin (OPG) and alkaline phosphatase (ALPL) in osteoblast-like SaOS2 cells cultured with MBG and

boron-containing MBG at the concentration of 1 mg mL^{-1}. No significant difference between the control and the particles in the expression of all the tested genes was observed after incubation for 72 h, whereas a major change in gene expression could be observed after 7 days of incubation. In comparison to the control, a downregulation of all pro-osteogenic genes was observed in SaOS2 cells cultured with MBG. The presence of boron further decreased the overall gene expression, with the lowest expression levels found following incubation with 10B-MBG, as compared to both the control and MBG. 15B-MBG also maintained a certain degree of low gene expression, with measured values slightly higher than those observed with 10B-MBG.

In this study, MBG (SiO$_2$-CaO composition) did not upregulate the expression of pro-osteogenic genes in comparison to the control, probably because the concentration of released ions from MBG at the dosage of 1 mg mL^{-1} could not trigger osteogenic differentiation of SaOS2 cells. It is known that active ions can only induce favorable biological responses at appropriate concentrations,[13] which means biological stimulation (including osteogenic activity) induced by BG is concentration- and time-dependent as well as being related to their chemical

Table 2. RANKL/OPG relative expression's ratio.

RANKL/OPG relative expression's ratio	72 h	7 d
Control	1.000	1.816
MBG	1.045	1.331
10B-MBG	1.124	4.383
15B-MBG	1.105	3.833

composition.[49] Moreover, it has been reported that BG nanoparticles with SiO_2-CaO composition could induce pro-osteogenic activities only when osteogenic differentiation supplements were added in the culture medium.[50] These reasons explain why MBG could not upregulate the expression of pro-osteogenic genes in SaOS2 cells. To achieve pro-osteogenic activities for bone regeneration applications, the dosage and chemical composition of MBG and boron-containing MBG should be optimized.

The downregulated expression of RANKL and OPG genes was observed in all experimental groups, and particularly boron-containing MBG induced the downregulation to a greater extent (Figure 6b). Furthermore, the observed expression values for RANKL and OPG in cells incubated with both 10B- and 15B-MBG at day 7 showed a RANKL/OPG ratio unbalanced toward RANKL (**Table 2**). RANKL is a cytokine produced by osteoblasts as a membrane-bound or a secreted protein that is involved in the regulation of osteoclast maturation and activity. OPG is a natural decoy receptor of RANKL and can counterbalance RANKL's action,[51] which plays a role in inhibiting osteoclastogenesis and bone resorption.[51] In comparison to the control and MBG, boron-containing MBG induced a higher RANKL/OPG ratio, which is the result of a reduced OPG expression rather than an increased RANKL expression. The extent of RANKL expression induced by boron-containing MBG was lower than those in the control and MBG. However, the significant reduction in OPG expression as compared to the control and MBG caused a RANKL/OPG's net contribution in favor of RANKL. Given that OPG expression increases with osteoblast differentiation while RANKL decreases,[52,53] these results support the hypothesis that boron-containing MBG could delay the osteoblast's differentiating phenotype while 10B-MBG showed the greatest effect in comparison to boron-free MBG.

The results of this study indicated that MBG, 10B-, and 15B-MBG were noncytotoxic, but these nanoparticles induced inflammatory response when cultured with macrophages. Notably, the incorporation of boron downregulated IL-1β and IL-6 expression, thus showing the ability of boron to reduce inflammatory action. Finally, boron-containing MBG exerted a downregulation of osteogenesis-related genes in osteoblast-like cells with an enhanced RANKL/OPG ratio, possibly implicated in early osteogenic differentiation stages and thus paving the way to possible applications in the field of bone regeneration under inflammatory conditions. The present preliminary in vitro biological assessment evidenced that the incorporation of boron in MBG could downregulate inflammatory cytokines and induce a parallel delay of the osteogenic process at the mRNA level. Future cell biology studies (e.g., Western blot) shall focus on understanding the influence of boron-containing MBG on the inflammatory and osteogenic activities at the protein level to expand the biological characterization of the developed nanoparticles.

3. Conclusion

Boron incorporated mesoporous bioactive glass nanoparticles (boron-containing MBG) were successfully synthesized by using a microemulsion assisted sol–gel approach. The particle size of boron-containing MBG was in the range of 100 to 300 nm. The incorporation of boron did not significantly affect the size and shape of the particles, but reduced the specific surface area and enlarged the mesopores toward wider pore size distribution. The concentration of boron incorporation could be adjusted by tuning the amount of boric acid added in the sol–gel process. The presence of boron in MBG did not significantly influence the high bioactivity of MBG. Both 10B- and 15B-MBG exhibited fast HA forming ability during soaking in SBF. Boron containing MBG showed no cytotoxicity against ST2 stromal cells at the concentrations of 1 and 0.1 mg mL^{-1}. Moreover, incorporation of boron into MBG reduced the inflammatory response in macrophages as confirmed by the downregulated expression of IL-1β and IL-6 genes. However, boron-containing MBG did not upregulate pro-osteogenic genes. The results show the feasibility of synthesizing boron-containing MBG by using boric acid as the precursor in the sol–gel process as well as the potential of boron incorporation in reducing inflammatory response induced by BG.

4. Experimental Section

Synthesis of Boron-Containing MBG: Boron containing MBG with nominal compositions of $50SiO_2$-$(50 - X)CaO$-XB_2O_3 (mol%; $X = 10$ and 15) as well as boron-free $60SiO_2$-$40CaO$ (mol%) were synthesized using a microemulsion-assisted sol–gel method as reported in the literature.[28,30] The resulting boron-containing particles were designated as 10B-MBG and 15B-MBG according to the concentration of boron, while the boron-free one was designated as MBG. In a typical synthesis procedure of 10B-MBG, 0.7 g of hexadecyl trimethyl ammonium bromide (CTAB; ≥ 97%, Merck) was dissolved in 33 mL of deionized water while stirring. After the solution became clear, 10 mL of ethyl acetate (≥99.8%, Merck) was added and the solution was stirred for 30 min. Then, 0.47 mL of aqueous ammonia (28%, VWR Chemicals) was added and stirred for another 15 min. 3.6 mL of tetraethyl orthosilicate (TEOS, 99%, Sigma-Aldrich), 3.06 g of calcium nitrate tetrahydrate (99.5%, VWR Chemicals), and 0.4 g of boric acid (H_3BO_3, ≥99.5%, Sigma-Aldrich) were sequentially added in intervals of 30 min. After the addition of boric acid, the mixtures were stirred for further 4 h. The particles were collected by centrifugation and washed twice with deionized water and once with ethanol (96%, VWR Chemicals). The collected particles were then dried at 60 °C overnight before calcination at 600 °C for 6 h with a heating rate of 2 °C min^{-1}. MBG and 15B-MBG were synthesized using the same method as described above with adjusted amounts of Ca and boron precursors corresponding to the nominal chemical compositions.

Particle Characterization: The morphology and microstructure of MBG, 10B-, and 15B-MBG were examined by scanning electric microscopy (SEM, Auriga, Zeiss, Germany) under an accelerating voltage of 2 kV. The particle size was determined according to SEM images using Image J (NIH, USA) and the number of counted particles was >300. The pore structure of the particles was assessed with transmission electron microscope (TEM, Philips CM30, Netherlands). For TEM observation, the particles were ultrasonically dispersed in ethanol and dropped on Cu grids. TEM images were then taken at an accelerating voltage of 300 kV.

MBG and boron-containing MBG were characterized by Fourier transform infrared spectroscopy (FTIR) (Shimadzu, IRAffinity-1S) to investigate their chemical structure. FTIR spectra were obtained in absorbance mode in the region of 400–2000 cm^{-1} spectrophotometer with

a resolution of 4 cm^{-1}. X-ray diffraction measurements were performed using a D8 ADVANCE X-ray diffractometer (Bruker, USA) in a 2θ range of 20°–80° with Cu Kα radiation. A step size of 0.02° with a dwell time of 1 s per step was used. The chemical composition of MBG and boron-containing MBG was determined by inductively coupled plasma atomic emission spectroscopy (ICP-AES, SPECTRO CIROS-CCP spectrometer). Briefly, the particles were first digested by using microwave heating, and 10 mL of concentrated HF/HNO$_3$/HCl mixture in 1/1/3 volume ratio was used as the digestion medium. The resulting samples were then diluted to 100 mL with deionized water for the analysis. The Brunauer–Emmett–Teller (BET) specific surface area (SSA) and Barrett–Joyner–Halenda (BJH) pore size distribution of MBG and boron-containing were determined by using the nitrogen sorption analysis, conducted on a Micromeritics porosimeter (ASAP2460, Micrometrics Instrument). Zeta potential and dynamic light scatting (DLS) nanoparticle size were measured using a Zetasizer Nano ZS (Malvern Instruments, UK). The samples were diluted with 10×10^{-3} M KCl aqueous solution to a concentration of 0.1 g L^{-1} for the DLS measurement while the zeta potential was measured in deionized water.

In Vitro Ion Release and Hydroxyapatite Formation: To evaluate the ion release of MBG and boron-doped MBG, 10 mg of each type of particle was dispersed in 20 mL of Tris-HCl buffer solution (pH 7.4) in an incubator (KS 4000i control, IKA, Germany) for up to 14 days at 37 °C shaking at 90 rpm. At each predetermined time point, 10 mL of the supernatant was collected by centrifugation and filtration. The samples were replenished with 10 mL of fresh Tris-HCl. The collected supernatants were then diluted and analyzed using ICP-AES to determine the concentrations of released Si, Ca, and B ions.

The in vitro bioactivity of MBG, 10B-, and 15B-MBG was accessed by soaking the nanoparticles in simulated body fluid (SBF) to observe the formation of hydroxyapatite (HA) according to the protocol proposed by Kokubo and Takadama.[42] Briefly, the particles were soaked in SBF at a concentration of 1 mg mL^{-1} and kept in an incubator at 37 °C shaking at 90 rpm. At predetermined time points, the samples were collected by centrifugation and washed once with deionized water and once with acetone (100%, VWR Chemicals). After drying, the samples were analyzed by FTIR, XRD, and SEM to observe the formation of HA. The characterization procedure was the same as described above.

Cell Culture: Mouse bone marrow stromal (ST2) cells (DSMZ GmbH, Germany), murine macrophages J774a.1 (BS TCL83), and osteoblast-like SAOS-2 (BS TCL 90) cells (IZSLER, Italy) were used in this study. ST2 cells were cultured in a humidified atmosphere of 95% air and 5% CO$_2$ at 37 °C in RPMI 1640 medium (Gibco, Germany) with 10 vol% fetal bovine serum (FBS; Sigma-Aldrich) and 1 vol% penicillin/streptomycin (Gibco, Germany). The cells were harvested before confluence by using a sterile trypsin-EDTA solution (0.5 g L^{-1} trypsin, 0.2 g L^{-1} EDTA in PBS, pH 7.4) (Life Technology, Carlsbad, USA. Macrophages were cultured in Dulbecco's modified Eagle's medium (DMEM; GIBCO, Life Technologies), supplemented with 10% FBS, penicillin (100 U mL^{-1}), streptomycin (100 μg mL^{-1}) and 4×10^{-3} M L-glutamine, at 37 °C in a 100% humidified incubator equilibrated with 10% CO$_2$. The cells were passaged 2–3 days before use. SAOS-2 cells were cultured in McCoy's 5A medium modified (GIBCO, Life Technologies) supplemented with 15% FBS, streptomycin (100 g L^{-1}), penicillin (100 U mL^{-1}), and 2 mmol L^{-1} L-glutamine at 37 °C in a humidified incubator equilibrated with 5% CO$_2$.

In Vitro Cytotoxicity

In Vitro Cytotoxicity—The WST Assay: MBG, 10B-, and 15B-MBG were sterilized at 160 °C for 2 h in a furnace (Nabertherm, Germany). 100 mg of each type of particles was added to 10 mL of cell culture medium to form a suspension (10 mg mL^{-1}) and pre-incubated at 37 °C for 24 h. After that, the suspension was collected and parts of them were diluted to form the other two suspensions at the concentrations of 1 and 0.1 mg mL^{-1}, respectively. ST2 cells were seeded in 24-well plates at the density of 1×10^5 cells mL^{-1} and incubated at 37 °C for 24 h. The culture medium was then removed and the suspension was added to each well before further incubation for 48 h. The cells cultured without particle suspensions were taken as a control. After 48 h of culture, the culture medium was removed and 400 μL of culture medium containing 1 vol% WST reagent (Sigma-Aldrich) was added to

the wells before a further culture of 2 h. Then 100 μL of the solution was uptake from each well and transferred to a 96-well plate. The supernatant was spectrometrically analyzed using a microplate reader (PHOmo, Anthos Microsystem GmbH) at 450 nm. The results were then converted to relative cell viability as shown below

$$\text{Relative cell viability} \, (\%) = \text{Sample} \, (\text{OD}) \, / \, \text{Control} \, (\text{OD}) \times 100\% \tag{1}$$

In Vitro Cytotoxicity—H&E Staining: To observe the morphology of the cells cultured with particles, Hematoxylin & Eosin (H&E) staining was performed. Briefly, after the WST assay, the remaining medium was removed from well plates and the attached cells were washed with PBS before being fixed by Fluoro-fix for 15 min. Subsequently, the fixed cells were washed with deionized water and stained with 0.5 mL of Hematoxylin for 20 min. After staining with Hematoxylin, the fixed cells were washed with tap water, followed by remaining in "Scott's tap water" for 10 min and then washed with deionized water to remove Hematoxylin. 0.5 mL of Eosin solution containing 0.4 wt% Eosin in 90% ethanol with 5% acetic acid was added to each well for 5 min. After staining with Eosin, the cells were washed with 95% and 100% ethanol to remove Eosin. All the stained cells were dried in a fume hood overnight and observed by light microscopy (Primo Vert, Carl Zeiss).

Expression of Proinflammatory Genes: Inflammatory responses of MBG and boron-containing MBG were investigated by culturing the particles with macrophages. Briefly, macrophages were seeded in 12-well plates containing the particles (1 mg mL^{-1}) at a density of 3×10^5 mL^{-1}. After 4 h of culture, the RNA from cells was isolated by using the Maxwell RSC simply RNA Cells Kit (Promega, Thermo Fisher Scientific, USA) and reverse transcribed by the High-Capacity cDNA Reverse Transcription Kit (Applied Biosystems, Thermo Fisher Scientific, USA). The real-time reverse transcription polymerase chain reaction (RT-qPCR) was performed on the Applied Biosystems QuantStudio 5 real-time PCR system (Thermo Fisher Scientific, USA). Mouse interleukin-1β (IL-1β), interleukin-6 (IL-6), tumor necrosis factor alpha (TNFα) and tyrosine 3-monooxygenase/tryptophan 5-monooxygenase activation protein zeta (YWHAZ) were chosen from the collection of the TaqMan Gene Expression Assays. The PCR primers used were obtained from Applied Biosystems and TaqMan probes assay IDs are listed in Table S1 (Supporting Information). RT-qPCR was performed for all samples according to the manufacturer's instruction. The content of cDNA samples was normalized through the comparative threshold cycle ($\Delta\Delta Ct$) method, consisting of the normalization of the number of target gene copies versus the endogenous reference gene YWHAZ. The group where cells were cultured in polystyrene wells without the addition of nanoparticles was treated as the control.

Expression of Pro-Osteogenesis Related Genes: Osteogenic responses of osteoblast-like SaOS-2 cells cultured with the particles were investigated. Briefly, the cells were cultured in 12-well plates at a density of 9.5×10^4 cells mL^{-1} while each well contained the Transwell insert (<0.3 μm, Sarstedt, Germany) with the particles added at the concentration of 1 mg mL^{-1}. After either 72 h or 7 d of incubation, the expression of glyceraldehyde-3-phosphate dehydrogenase (GAPDH), collagen 1A1 (COL1A1), receptor activator of nuclear factor kappa-B ligand (RANKL), secreted protein acidic and cysteine rich (SPARC), osteoprotegerin (OPG) and alkaline phosphatase (ALPL) genes, as cell osteogenic differentiation markers, was assessed by RT-qPCR according to the manufacturer's instruction. The primers used are listed in Table S1 (Supporting Information). The RNA from SAOS-2 cells was isolated by using the Maxwell RSC simply RNA Cells Kit. RNA was reverse transcribed by the High-Capacity cDNA Reverse Transcription Kit and RNA quantitation was performed before starting the RT-qPCR in the Quantus Fluorometer (Promega, Thermo Fisher Scientific, USA), by using the Quantifluor system kit (Promega, Thermo Fisher Scientific, USA). The content of cDNA samples was normalized to the endogenous reference gene GAPDH by using the $\Delta\Delta Ct$ method. The group where cells were cultured in polystyrene wells without the addition of nanoparticles was treated as the control.

Statistical Analysis: Quantitative data are reported as mean value ± standard deviation (S.D.) from at least two independent experiments. Statistical differences (in RTqPCR analysis) between groups were analyzed using the two-way ANOVA statistical test, with Tukey's post-hoc test and the one-way ANOVA, with Tukey's pairwise post-hoc test. Bonferroni's post hoc test was used to analyze the statistical significance in the cell viability test. Statistical significance is represented as $*p < 0.05$, $**p < 0.01$, $***p < 0.001$ and $****p < 0.0001$.

Supporting Information

Supporting Information is available from the Wiley Online Library or from the author.

Acknowledgements

Conflict of Interest

The authors declare no conflict of interest.

Keywords

bioactive glasses, bioactivity, boron, inflammatory response, osteogenic activity

[1] T. Winkler, F. A. Sass, G. N. Duda, K. Schmidt-Bleek, *Bone Jt. Res.* **2018**, *7*, 232.

[2] G. Fernandez de Grado, L. Keller, Y. Idoux-Gillet, Q. Wagner, A. M. Musset, N. Benkirane-Jessel, F. Bornert, D. Offner, *J. Tissue Eng.* **2018**, *9*, 204173141877681.

[3] A. A. El-Rashidy, J. A. Roether, L. Harhaus, U. Kneser, A. R. Boccaccini, *Acta Biomater.* **2017**, *62*, 1.

[4] L. L. Hench, *Biomed. Glasses* **2015**, *1*, 1.

[5] J. R. Jones, *Acta Biomater.* **2015**, *23*, S53.

[6] K. Zheng, A. R. Boccaccini, *Adv. Colloid Interface Sci.* **2017**, *249*, 363.

[7] Y. Zhang, L. Xia, D. Zhai, M. Shi, Y. Luo, C. Feng, B. Fang, J. Yin, J. Chang, C. Wu, *Nanoscale* **2015**, *7*, 19207.

[8] K. Zheng, N. Taccardi, A. M. Beltran, B. Sui, T. Zhou, V. R. R. Marthala, M. Hartmann, A. R. Boccaccini, *RSC Adv.* **2016**, *6*, 95101.

[9] L. Weng, S. K. Boda, M. Teusink, F. D. Shuler, X. Li, J. Xie, *ACS Appl. Mater. Interfaces* **2017**, *9*, 24484.

[10] V. Miguez-Pacheco, L. L. Hench, A. R. Boccaccini, *Acta Biomater.* **2015**, *13*, 1.

[11] S. Kargozar, M. Montazerian, S. Hamzehlou, H. W. Kim, F. Baino, *Acta Biomater.* **2018**, *81*, 1.

[12] C. Wu, J. Chang, *J. Controlled Release* **2014**, *193*, 282.

[13] A. Hoppe, N. S. Güldal, A. R. Boccaccini, *Biomaterials* **2011**, *32*, 2757.

[14] H. Khaliq, Z. Juming, P. Ke-Mei, *Biol. Trace Elem. Res.* **2018**, *186*, 31.

[15] P. Balasubramanian, T. Büttner, V. Miguez Pacheco, A. R. Boccaccini, *J. Eur. Ceram. Soc.* **2018**, *38*, 855.

[16] Q. Yang, S. Chen, H. Shi, H. Xiao, Y. Ma, *Mater. Sci. Eng., C* **2015**, *55*, 105.

[17] S. Zhao, L. Li, H. Wang, Y. Zhang, X. Cheng, N. Zhou, M. N. Rahaman, Z. Liu, W. Huang, C. Zhang, *Biomaterials* **2015**, *53*, 379.

[18] R. Moonesi Rad, A. Z. Alshemary, Z. Evis, D. Keskin, K. Altunbaş, A. Tezcaner, *Ceram. Int.* **2018**, *44*, 9854.

[19] R. Moonesi Rad, D. Atila, Z. Evis, D. Keskin, A. Tezcaner, *J. Tissue Eng. Regener. Med.* **2019**, *13*, 1331.

[20] V. K. Parashar, J.-B. Orhan, A. Sayah, M. Cantoni, M. A. M. Gijs, *Nat. Nanotechnol.* **2008**, *3*, 589.

[21] S. Labbaf, O. Tsigkou, K. H. Müller, M. M. Stevens, A. E. Porter, J. R. Jones, *Biomaterials* **2011**, *32*, 1010.

[22] D. Shen, J. Yang, X. Li, L. Zhou, R. Zhang, W. Li, L. Chen, R. Wang, F. Zhang, D. Zhao, *Nano Lett.* **2014**, *14*, 923.

[23] F. Zhao, B. Lei, X. Li, Y. Mo, R. Wang, D. Chen, X. Chen, *Biomaterials* **2018**, *178*, 36.

[24] T. H. Kim, M. S. Kang, N. Mandakhbayar, A. El-Fiqi, H. W. Kim, *Biomaterials* **2019**, *207*, 23.

[25] K. Zheng, E. Torre, A. Bari, N. Taccardi, C. Cassinelli, M. Morra, S. Fiorilli, C. Vitale-Brovarone, G. Iviglia, A. R. Boccaccini, *Mater. Today Bio* **2020**, *5*, 100041.

[26] C. D. Hunt, J. P. Idso, *J. Trace Elem. Exp. Med.* **1999**, *12*, 221.

[27] X. Lu, K. Li, Y. Xie, S. Qi, Q. Shen, J. Yu, L. Huang, X. Zheng, *J. Biomed. Mater. Res., Part A* **2019**, *107*, 12.

[28] Q. Liang, Q. Hu, G. Miao, B. Yuan, X. Chen, *Mater. Lett.* **2015**, *148*, 45.

[29] Z. Neščáková, K. Zheng, L. Liverani, Q. Nawaz, D. Galusková, H. Kaňková, M. Michálek, D. Galusek, A. R. Boccaccini, *Bioact. Mater.* **2019**, *4*, 312.

[30] K. Zheng, J. Kang, B. Rutkowski, M. Gawęda, J. Zhang, Y. Wang, N. Founier, M. Sitarz, N. Taccardi, A. R. Boccaccini, *Front. Chem.* **2019**, *7*, 1.

[31] Q. Nawaz, M. Atiq, U. Rehman, A. Burkovski, J. Schmidt, A. M. Beltrán, A. Shahid, N. K. Alber, W. Peukert, A. R. Boccaccini, *J. Mater. Sci.: Mater. Med.* **2018**, *29*, 64.

[32] X. Kesse, C. Vichery, J.-M. Nedelec, *ACS Omega* **2019**, *4*, 5768.

[33] J. Yang, W. Chen, X. Ran, W. Wang, J. Fan, W. X. Zhang, *RSC Adv.* **2014**, *4*, 20069.

[34] J. Zhang, M. Liu, C. Song, X. Guo, *Microporous Mesoporous Mater.* **2011**, *139*, 31.

[35] Y. Li, X. Chen, C. Ning, B. Yuan, Q. Hu, *Mater. Lett.* **2015**, *161*, 605.

[36] K. Zheng, X. Dai, M. Lu, N. Hüser, N. Taccardi, A. R. Boccaccini, *Colloids Surf., B* **2017**, *150*, 159.

[37] S. L. Greasley, S. J. Page, S. Sirovica, S. Chen, R. A. Martin, A. Riveiro, J. V. Hanna, A. E. Porter, J. R. Jones, *J. Colloid Interface Sci.* **2016**, *469*, 213.

[38] S. Lin, C. Ionescu, K. J. Pike, M. E. Smith, J. R. Jones, *J. Mater. Chem.* **2009**, *19*, 1276.

[39] H. Aguiar, J. Serra, P. González, B. León, *J. Non-Cryst. Solids* **2009**, *355*, 475.

[40] R. Lucacel Ciceo, D. L. Trandafir, T. Radu, O. Ponta, V. Simon, *Ceram. Int.* **2014**, *40*, 9517.

[41] Q. Fu, M. N. Rahaman, H. Fu, X. Liu, *J. Biomed. Mater. Res., Part A* **2010**, *95A*, 164.

[42] T. Kokubo, H. Takadama, *Biomaterials* **2006**, *27*, 2907.

[43] A. L. B. Maçon, T. B. Kim, E. M. Valliant, K. Goetschius, R. K. Brow, D. E. Day, A. Hoppe, A. R. Boccaccini, I. Y. Kim, C. Ohtsuki, T. Kokubo, A. Osaka, M. Vallet-Regí, D. Arcos, L. Fraile, A. J. Salinas, A. V. Teixeira, Y. Vueva, R. M. Almeida, M. Miola, C. Vitale-Brovarone, E. Verné, W. Höland, J. R. Jones, *J. Mater. Sci.: Mater. Med.* **2015**, *26*, 115.

[44] P. V. Seredin, D. L. Goloshchapov, T. Prutskij, Y. A. Ippolitov, *Results Phys.* **2017**, *7*, 1086.

[45] M. Mačković, A. Hoppe, R. Detsch, D. Mohn, W. J. Stark, E. Spiecker, A. R. Boccaccini, *J. Nanoparticle Res.* **2012**, *14*, 966.

ADVANCED
SCIENCE NEWS
www.advancedsciencenews.com

Particle
& Particle Systems Characterization
www.particle-journal.com

[46] P. Balasubramanian, A. Grünewald, R. Detsch, A. R. Boccaccini, L. Hupa, B. Jokic, F. Tallia, A. K. Solanki, J. R. Jones, *Int. J. Appl. Glas. Sci.* **2016**, *7*, 206.

[47] E. J. Park, K. Park, *Toxicol. Lett.* **2009**, *184*, 18.

[48] U. Acaroz, S. Ince, D. Arslan-Acaroz, Z. Gurler, I. Kucukkurt, H. H. Demirel, H. O. Arslan, N. Varol, K. Zhu, *Food Chem. Toxicol.* **2018**, *118*, 745.

[49] J. Isaac, J. Nohra, J. Lao, E. Jallot, J. M. Nedelec, A. Berdal, J. M. Sautier, *Eur. Cells Mater.* **2011**, *21*, 130.

[50] O. Tsigkou, S. Labbaf, M. M. Stevens, A. E. Porter, J. R. Jones, *Adv. Healthcare Mater.* **2014**, *3*, 115.

[51] B. F. Boyce, L. Xing, *Arthritis Res. Ther.* **2007**, *9*, S1.

[52] F. Gori, L. C. Hofbauer, C. R. Dunstan, T. C. Spelsberg, S. Khosla, B. Lawrence Riggs, *Endocrinology* **2000**, *141*, 4768.

[53] G. J. Atkins, P. Kostakis, B. Pan, A. Farrugia, S. Gronthos, A. Evdokiou, K. Harrison, D. M. Findlay, A. C. W. Zannettino, *J. Bone Miner. Res.* **2003**, *18*, 1088.